# Chapter 4

# Studies of Single-Crystal Surfaces with Small Adsorbates *

The UEC experiments for surface studies were first demonstrated on semiconductor surfaces, such as silicon and GaAs. They are ideal systems because the surfaces can be relatively easily prepared with different absorbates, and their crystalline and physical properties are well studied. There have been a wide range of ultrafast optical experiments (for reviews, see reference [47, 48]), as well as recent ultrafast X-ray experiments revealing bulk lattice dynamics following fs laser excitation (see reference [5] for a review). It has been shown that the energy transfer to the lattice on the ps time scale by electron-phonon coupling, first to optical phonons then to acoustic phonons, and the stress created by impulsive excitation leads to lattice waves. However, the ultrafast X-ray experiments could not probe the surface owing to the large penetration depth into the crystal, typically up to several $\mu$m, which is also much larger than the nm scale penetration depth of the pump laser. On the other hand, optical techniques that probed the surface on the scale of a few nm and matched the exact pumped region, could not directly determine the structure with atomic-scale resolution, but gave valuable information on the response of the dielectric function and lattice disordering [49, 50, 48]. The large scattering cross section of electrons combined with ultrafast time resolution allows the bridging of this gap in addressing the dynamics of surface structures in real time, and provides new insight to the dynamics of the surface absorbates.

---

*This chapter is based on the work presented in references [24, 25].

## 4.1 Silicon(111) surface

Silicon crystal structure is the diamond tetrahedral type [51] and the (111) surface is the most densely packed crystal plane, as depicted in figure 4.1. The bare surface is not stable in air because of the dangling bond and is easily oxidized. The Si(111) surface can be hydrogen terminated by standard method, or be terminated by other atoms or molecules, such as the halogens or a methyl group [52]. In our experiments, Si(111):H surfaces were prepared from wafers, first by cleaning and oxidation with an RCA-1 solution, then by etching in a 40% $NH_4F$ solution for 15 to 20 minutes. And the surface quality was independently checked by LEED and Auger Spectroscopy.

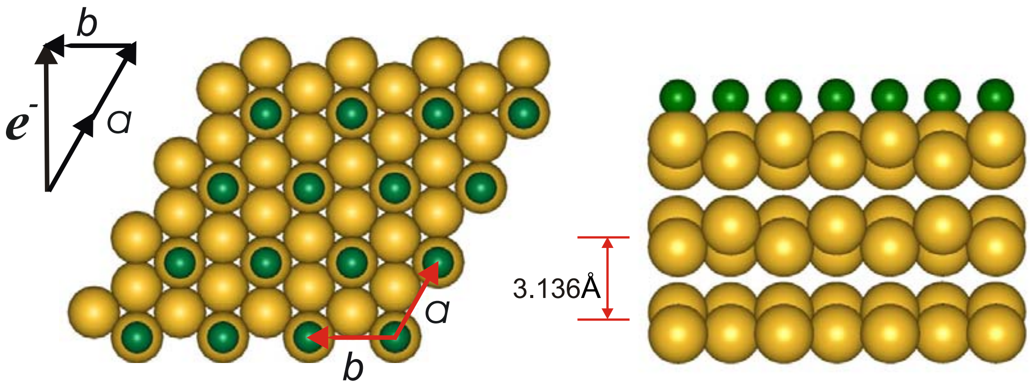

Figure 4.1: Structure of the Hydrogen-terminated Si(111) crystal, with the bilayer spacing of 3.136 Å [24].

Figure 4.2 shows the static diffraction patterns of different Si(111) surfaces, obtained by using the ultrashort electron pulses, but without the initiating pumping laser pulse. And it is equivalent to the diffraction patterns obtained when the electron pulse arrive before the laser pulse, i.e., $t < 0$. Figure 4.2 displays the very strong (0,0) streak, and other Bragg reflections in zero and first Laue zones, from a hydrogen terminated Si(111) surface. It demonstrates the high quality of the single-crystal surface, and the surface structure is determined to be (1×1) Si(111). The rocking curves are obtained by varying the incidence angle $\theta_i$, as part of the rocking curve is shown in figure 4.3. From the Bragg angles the bilayer distance is determined.

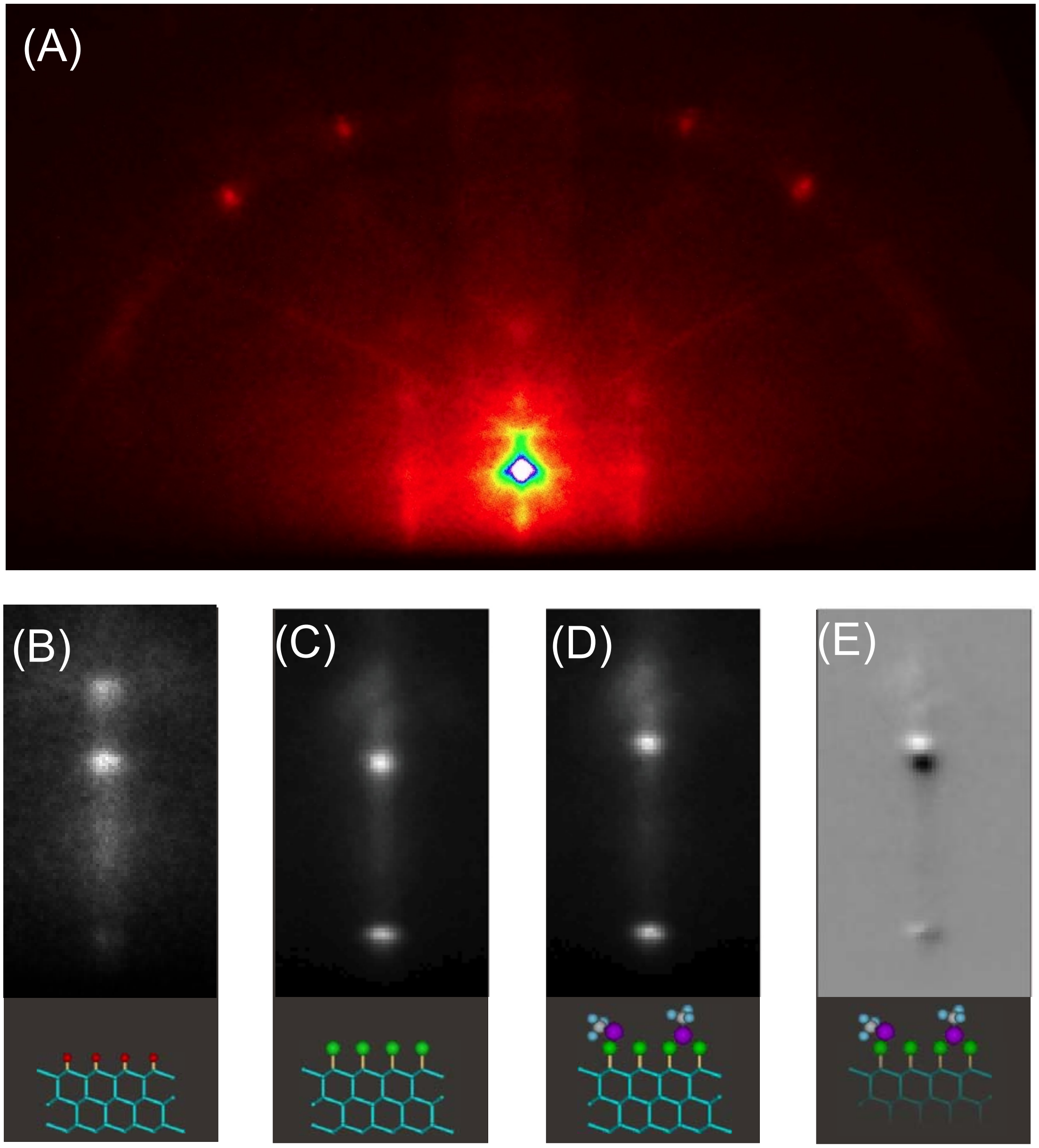

Figure 4.2: Diffraction patterns of Si(111) surfaces. (A) The pattern of hydrogen-terminated silicon in the in-phase condition. (B) A close-up of the (0,0) streak in the out-of-phase condition. Also shown are the changes in the streak region for chemisorbed chlorine (C) and physisorbed trifluroiodomethane (D). The difference (D)-(C) enhances the diffraction change purely induced by coverage of trifluroiodomethane (E) [24].

It is shown that in the out-of-phase condition, i.e., $\theta_i$ does not equal the Bragg angle, in the low angles ($\theta_i < 2°$) the intensity of the (0,0) streak is modulated to show two peaks. These two peaks are very sensitive to the surface condition, as shown in figure 4.2, and changes from hydrogen terminated to chlorine terminated, to a physisorbed trifluroiodomethane structure, which was obtained by continuously dosing 99% pure gaseous trifluroiodomethane at $\sim 10^{-6}$ torr at the sample through the gas doser. As such, they are also very sensitive to the surface structural change in the ultrafast time scale. To calculate the diffraction intensity modulation requires the inclusion of multiple scattering in a dynamical theory. However, the kinematical modeling can reproduce the basic features of the (0,0) streak [24]. For hydrogen termination, it is calculated from the diffraction pattern that the silicon atoms of the top bilayer on the surface contract by 0.08 Å from that of the bulk, in agreement with *ab initio* theoretical analysis [53].

Figure 4.3 displays the time dependent rocking curves of the Bragg spot (-4,7), which is a side peak at the first Laue zone and the notation follows the chosen $\vec{a}$ and $\vec{b}$ in figure 4.1. As shown in figure 4.3(A), at higher $\theta_i$, the side spot's position changes as an effect of the incidence Bragg angle. Figure 4.3(B) shows that the shift and width of the Bragg peak behave differently but consistently, with the delay needed for the creation of the lattice phonons [48]. The width increases to its maximum value ($\Delta\theta = 0.08°$), but then decays with the time constant indicated (40 ps). The shift, however, has a finite rise comparable to the time it takes the broadening to lose almost 80% of its maximum value. Accordingly, the initial stress created in the substrate leads to an inhomogeneous compression and expansion which result in the known broadenings (by coherent phonons [54]) of the rocking curves. As the lattice reaches its maximum expansion, with the decay of inhomogeneity due to the loss of coherence of acoustic phonons, the shift reaches it maximum value; at longer times, both broadening and shift recover the values of the equilibrium structure. The maximum expansion, following the decay of acoustic phonons, is observed at $\theta_i = 3.06°$, which corresponds to a 1.7% (0.04 Å) increase for the Si-Si distance at 2.35 Å. Even at the maximum shift, there is still an interplay between energy redistribution and cooling. At the point of levelling off (figure 4.3(B)), the shift (0.015 Å) defines a lattice temperature of ∼ 1500 K, just below melting (1687 K).

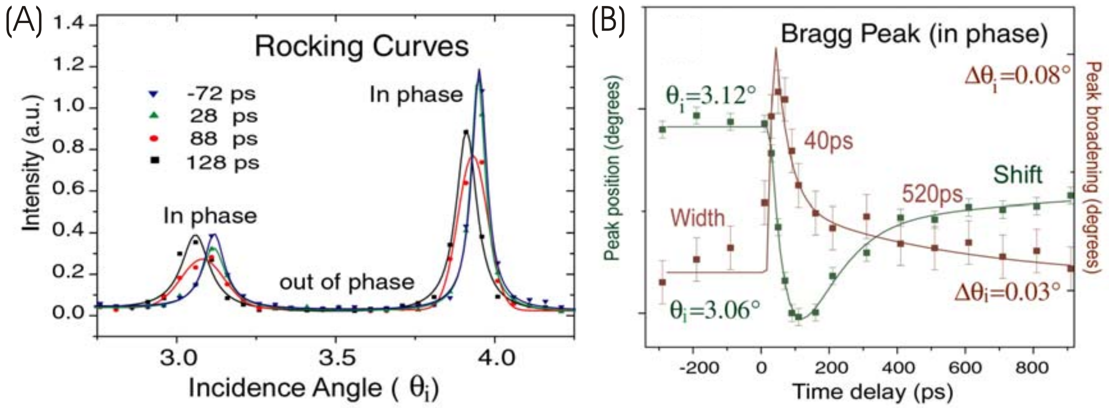

Figure 4.3: The temporal change of the Bragg spot (-4,7). (A) The temporal profile of the rocking curves for the (-4,7) Bragg spot. Note only four data points are shown to illustrate the dynamical changes. (B) The brown and green curves give the time-dependence of the angular width and position of the Bragg spot (-4,7) by following the rocking curves in panel (A) [24].

These studies were also extended to chemisorption (hydrogen and chlorine atoms) and physisorption (trifluroiodomethaneon molecules) on silicon surfaces in order to elucidate the effect of surface motion and the potential of the absorbed atoms or molecules. On going from hydrogen to chlorine, the amplitude of the atomic motion decrease to ∼0.1 Å. The temporal response of the chlorine system is similar in trends to that of hydrogen but significantly slower to be 110 ps. Two processes might be in effect here; first the heavier mass of chlorine compared to hydrogen, and second the high electronegativity. Trapping of electrons, with the change in the available energy, modifies the potential and also requires additional nuclear motions of the adsorbates. The adsorption of molecular trifluroiodomethane shortens the decay, consistent with a reduced effective electronegativity due to the physisorption of the molecules.

The structural changes involved in phase transitions were studied, when the temperature of the lattice is high enough to cause large amplitude disorder. This critically depends on the density of the excited carries. Studies were performed at different excitation fluences (800nm and 266nm), and it was found that the maximum impulsive surface motion of atoms emerges when the carrier density is about a factor 2–5 below $10^{22}$ cm$^{-3}$, the threshold for melting. At carrier densities of $5 \times 10^{20}$ cm$^{-3}$ and below, the surface response is slower and the amplitude of structure change is linear with energy fluence. From bulk structural point of view, melting is defined by the Lindemann limit [55] which sets a 10% lattice change as the threshold for disorder. However, it is not clear that the limit is applicable to surface and mesoscopic melting [56]. In UEC experiments, irradiation of crystalline silicon with infrared pulses for a few hours, just below the damage threshold, results in amorphous silicon. The loss of the crystalline to the amorphous structure was evident in the disappearance of the intense Bragg spots and the appearance of smooth rings in our diffraction images (figure 4.4(A)).

Infrared fs pulse excitation of this amorphous structure gives new diffraction ring patterns, which we followed as a function of time. The instantaneous structural change is a phase transition to the liquid state. This is evident in the change of the radial distribution function, as we observe a depletion of the density of the second coordination shell at ∼4.3 Å, while the density of the first coordination shell at 2.35 Å remains the same. Unlike crystalline silicon, amorphous silicon is best described by a continuous random network model [57], in which atoms are topologically connected with fourfold coordination, but with the bond angles fluctuating substantially around 109.5°, the tetrahedron angle. And the first two coordination shells of the radial distribution function around 2.4 and 4 Å, respectively [58]. In the liquid phase, the bond angle fluctuations are further enhanced, and the radial distribution function shows almost no second coordination shell [59].

The amorphous-to-liquid phase transition occurs in ∼10 ps and the amorphous structure is recovered on a much different time scale (figure 4.4(C)). However, the liquid phase persists for ∼100 ps, as evident from the plateau. The persistence of the liquid phase indicates that the surface layers probed by the electrons remain very hot, being unable to dissipate the thermal excess energy. We note that the time scale reported here for the phase transition is different from that of the crystalline-to-liquid silicon, measured by reflection methods [60] and that the restructuring occurs on a

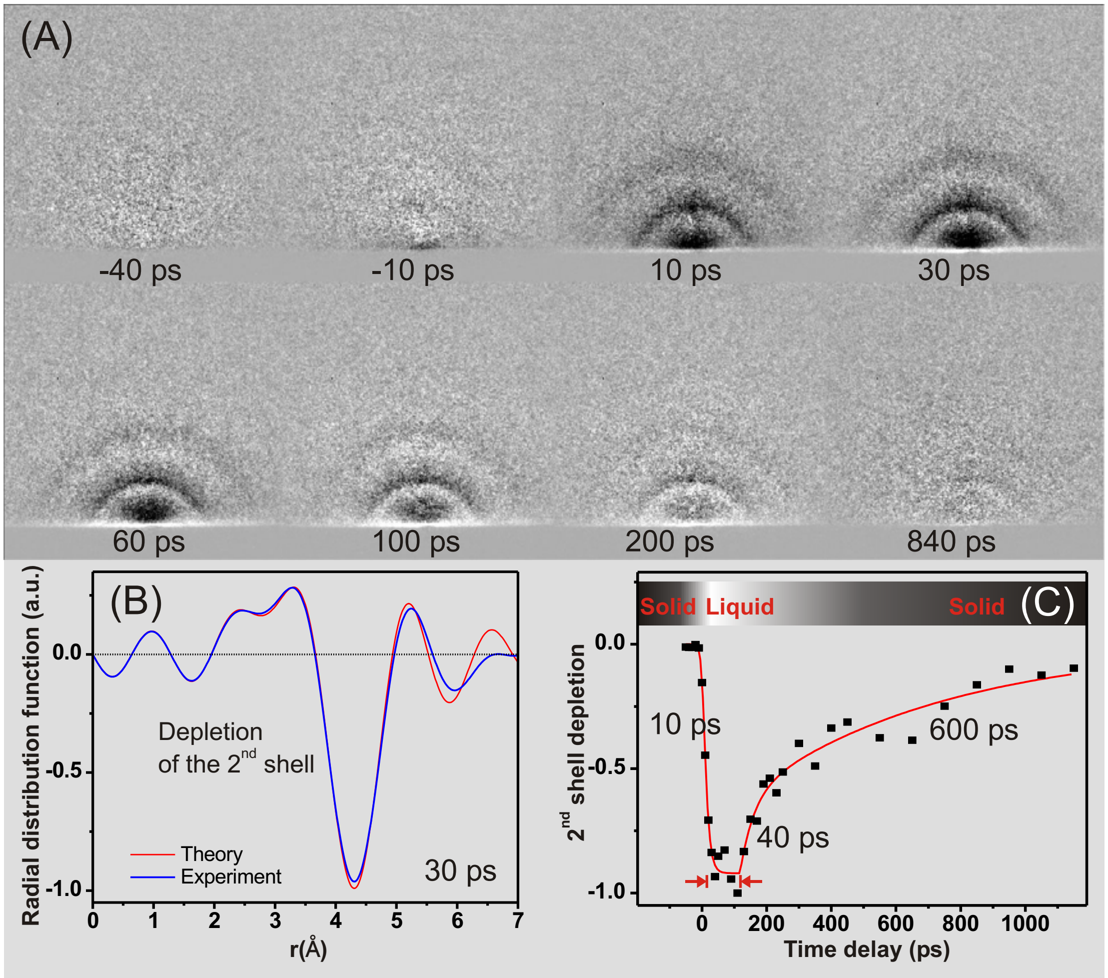

Figure 4.4: UEC of phase transition of the amorphous to liquid state. (A) Diffraction difference patterns at various time delays. From the patterns, we obtained a "molecular" scattering function and by Fourier transform the radial distribution function (shown in (B) for $t = +30$ ps). (C) The time dependence of the depletion and recovery of the second shell shows the ultrafast melting, followed by a ∼100 ps plateau, and later by resolidification (∼40 ps and ∼600 ps) [24].

time scale much shorter than typically reported for equilibration (ns or longer)[61]. Recent *ab initio* molecular dynamics simulations of silicon melting [62] have elucidated that ultrafast structural changes can lead to a new liquid structure characterized by a high coordination number and strong reduction of covalent bonding. This leads to significant changes in the shape of the pair correlation function $g(r)$ around ∼4 Å. We have observed the time evolution of the peak at ∼4.3 Å toward shorter distances (the second shell is at 3.8 Å in the amorphous solid and 3.6 Å in the liquid [58, 59]).

## 4.2 GaAs(111) surface

The GaAs is of Zinc Blend structure. Unlike Silicon, it is a semiconductor with direct bandgap [63]. The GaAs(111) surface was prepared following the procedure of reference [64]. The semi-insulating GaAs(111) crystals were terminated by a monolayer of chlorine with a Cl atom atop each Ga atom, saturating the otherwise dangling bond of Ga (figure 4.5). The surface retained its integrity throughout the experiments, as evidenced by the unchanged quality of the diffraction patterns.

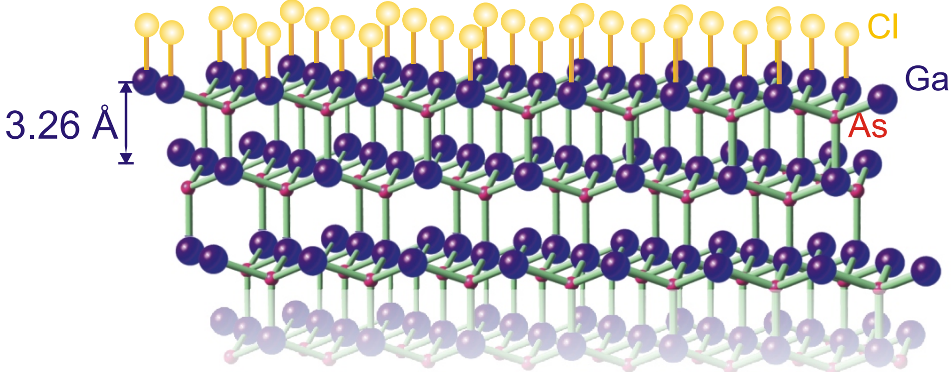

Figure 4.5: Structure of the chlorine-terminated GaAs(111) crystal, with the bilayer spacing of 3.26 Å [25].

The two-dimensional surface structure is shown in figure 4.6. Figure 4.6(A) displays the real space crystal lattice, with the atomic spacing of $a = b = 4.00$ Å. The samples were positioned to allow the electron beam to impinge at the chosen incidence angle ($\theta_i < 5°$), azimuthally along the $< 11\bar{2} >$ direction. Figure 4.6(B) displays the corresponding reciprocal lattice, with $a^* = b^* = 0.289$ Å$^{-1}$. The lattice basic vectors can also be chosen as $\vec{X}$ and $\vec{Y}$, and the reciprocal vectors are $\vec{X}^*$ and $\vec{Y}^*$, where $\vec{X}^*$ is perpendicular to the electron incidence and $\vec{X}^* = \sqrt{3}a^* = 0.499$ Å$^{-1}$. The Ewald sphere of radius $k = \lambda^{-1} = 14.33$ Å$^{-1}$ intersects with the reciprocal lattice as shown in figure 4.6(B). LZ0, LZ1 and LZ2 refer to the zero-order, first-order and second-order Laue zones.

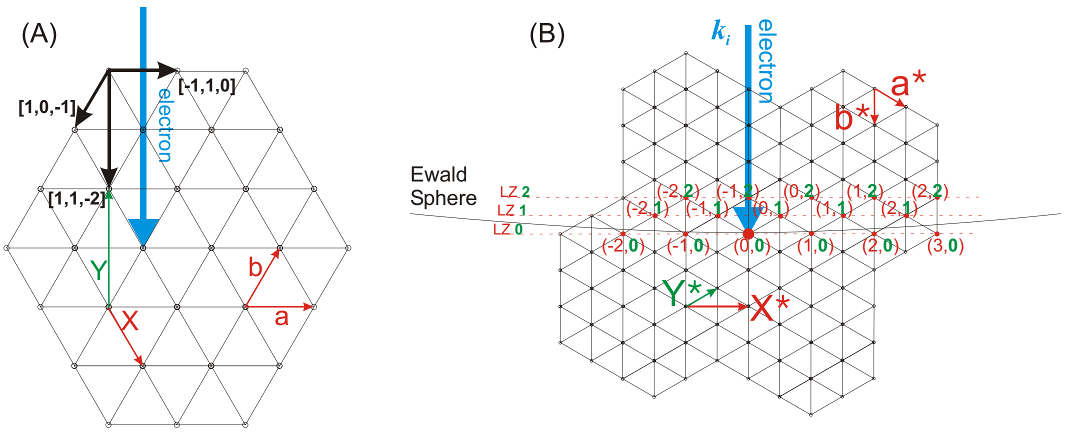

Figure 4.6: GaAs:Cl(111) surface lattice (A) in real space and (B) in reciprocal space.

Figure 4.7 presents a typical static diffraction image, which displays the very strong (0,0) and other Bragg reflections. Figure 4.7(A) shows a diffraction pattern, with such incidence angle as to reveal higher order diffraction peaks as well as diffraction streaks in the zero-order Laue zone. These and similar data allow for the precise determination of the camera distance from the scattering position (170 ± 1 mm).

By gating the detection on the (0,0) Bragg spot and following the diffraction position as a function of the incidence angle, we also obtained the experimental rocking curve, which gives the GaAs lattice periodicity along the (111) direction ($n = 1, 2, \dots$). This is shown in figure 4.7(B), where the incidence angle was varied over several degrees. The experimental periodicity in $\theta_i$ of 0.60°± 0.02° is in quantitative agreement with the expected value of 0.61° obtained for the lattice bilayer

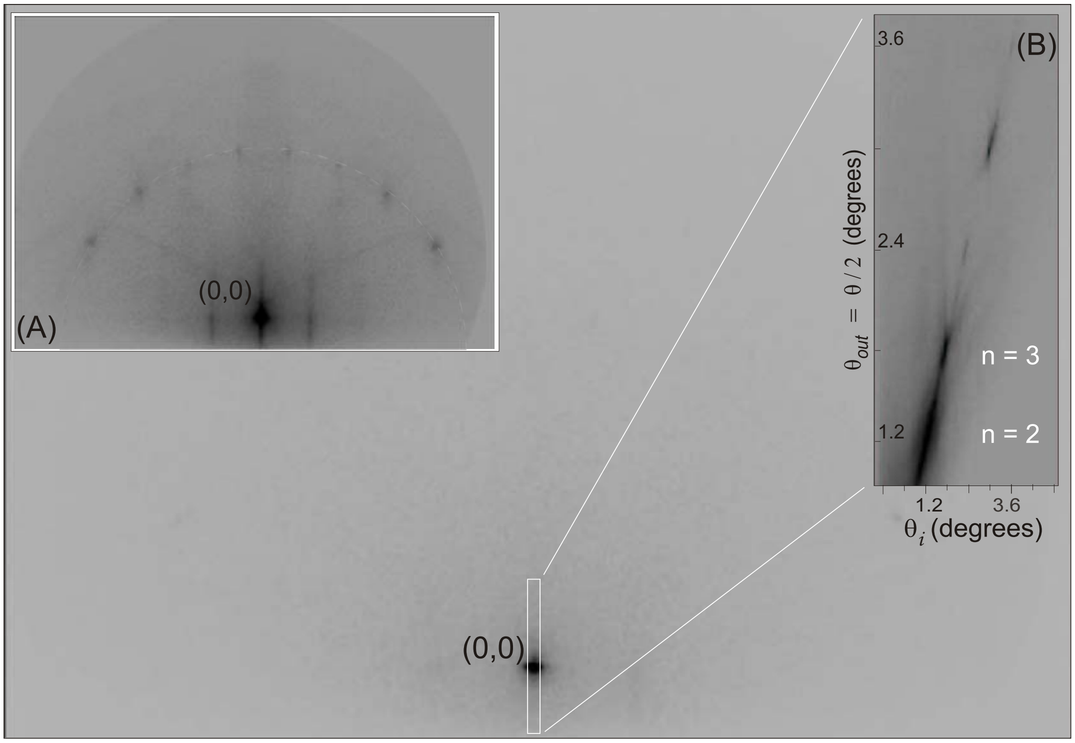

Figure 4.7: Static diffraction images of the GaAs:H(111) surface obtained by the ultrashort electron pulses. (A) Diffraction image showing the intense (0,0) in-phase reflection, together with the streaks and spots in the Laue zones. (B) Experimental rocking curve for the (0,0) reflection — (111) lattice planes. Note the image intensity is inverted [25].

spacing of 3.26 Å.

In the time-resolved experiment, the excitation laser of 266nm (400 $\mu$J, <300 fs) is used. This UV pulse at $t = 0$ defines the initial temperature and structural change. We follow the center position, intensity and the width of the $n = 2$ (0,0) Bragg spot as a function of time.

The change of the peak center position maps out the change of lattice spacing in the (111) direction, as shown for two different laser excitation powers in figure 4.8. Results are shown for fluences of 9% and 45% of the experimentally determined 4.5 mJ/cm$^2$ damage threshold at 266nm. The angular deviation ($\Delta\theta$) of the Bragg spot directly gives the change in lattice spacing ($\Delta d_{111}$), from the relation $\Delta d_{111} = -\frac{\Delta\theta \cdot d_{111}}{2sin(\theta/2)}$ here $\theta$ is the total scattering angle. A deviation to larger or smaller angles ($\Delta\theta > 0$ or $\Delta\theta < 0$) is therefore the signature of lattice contraction or expansion.

From the results shown in figure 4.8, it is evident that, following excitation at $t = 0$, the top surface layers of the crystal immediately contract. The amplitude of this initial contraction is given for two fluences, but the complete fluence dependence is presented in figure 4.9. After the initial contraction (-0.015 Å), the system expands to a maximum amplitude: +0.025 Å for fluence of 2 mJ/cm$^2$ and +0.005 Å for fluence of 0.4 mJ/cm$^2$. As can be seen from figure 4.9, the maximum expansion amplitude strongly depends on the fluence: the larger the fluence the more ample the expansion. The data also show that both the onset time and the velocity of the expansion ($\sim$m/s) strongly depend on the fluence: expansion occurs earlier and faster at the higher fluences. After reaching its maximum expansion, the system contracts again toward the original lattice spacing on a much longer time scale, beyond 50 ps, but a finite smaller expansion persists for at least several ns. Observations were also made for 800nm fs excitation at various laser fluences and the behavior is similar, namely an initial contraction, followed by an expansion and the subsequent return toward the initial lattice spacing. This similarity in form indicates that the observed structural dynamics is not dominated by a charging of the surface by photoemission, since excitation at 800nm and/or at low fluences gives similar behaviors.

The transient temperature is evident in the change of the diffraction integrated

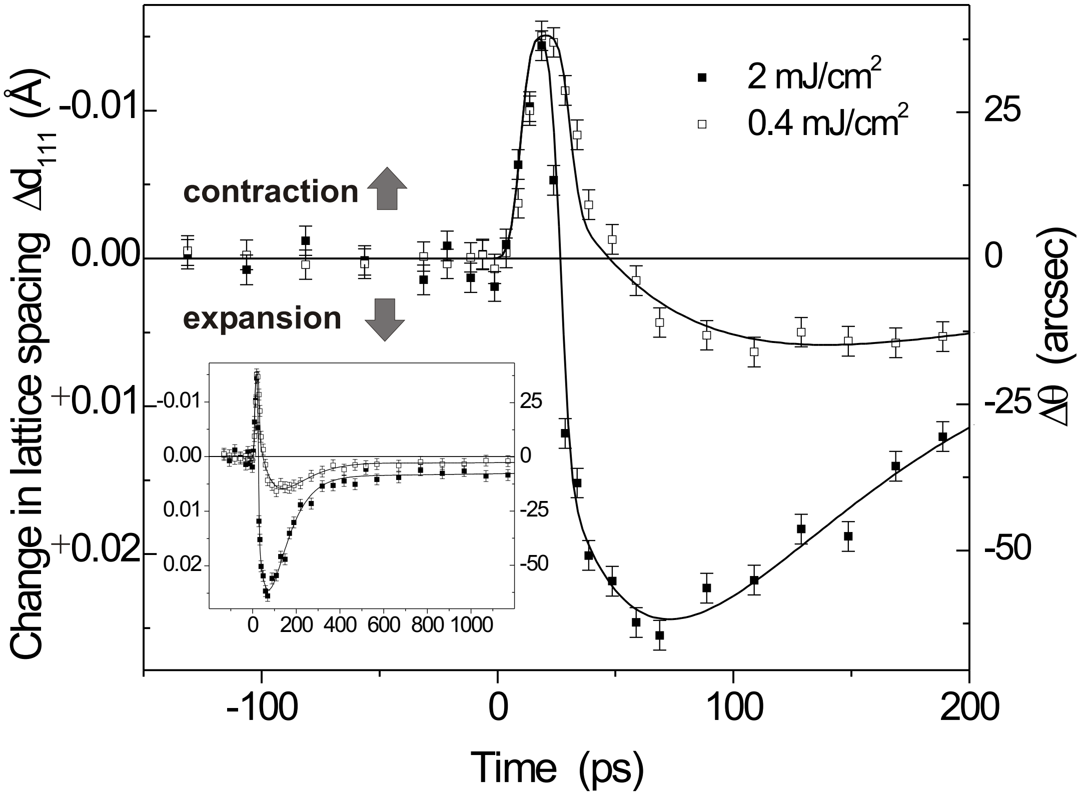

Figure 4.8: Center position of the Bragg spot as a function of time and fluence. The vertical axis on the right gives the angular deviation and the left axis shows the corresponding change in lattice spacing, perpendicular to the (111) surface plane. The inset shows the evolution at long time [25].

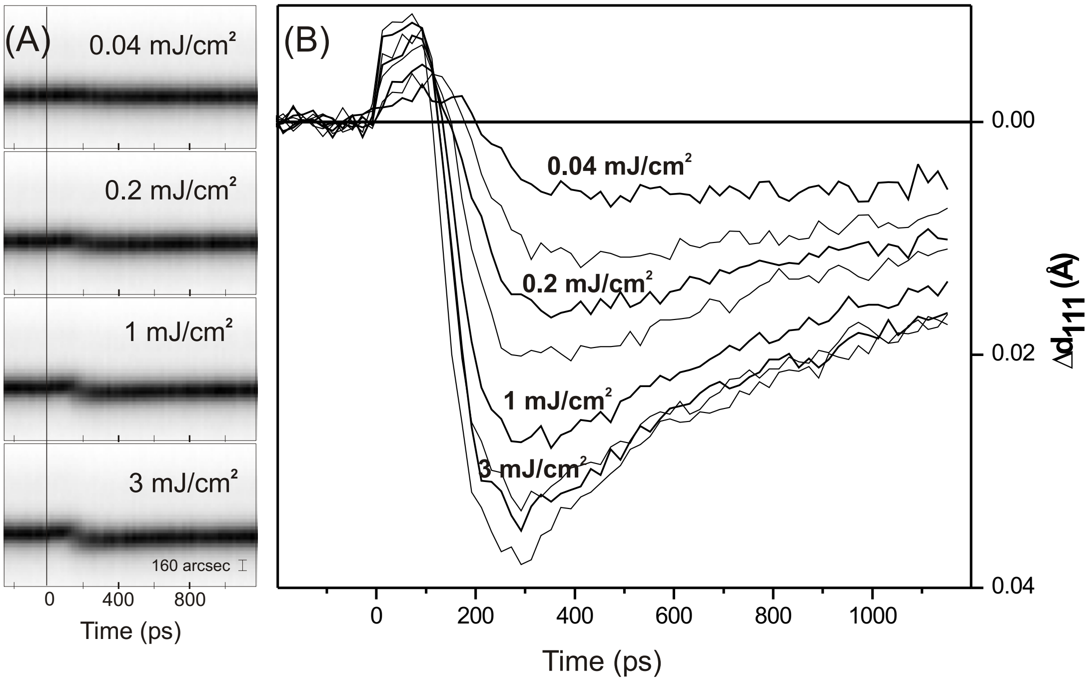

Figure 4.9: Fluence dependence of the Bragg reflection center position change. (A) Experimental traces for a set of data at the indicated fluences. (B) Time dependence of $\Delta d_{111}$, corresponding to the Bragg reflection center position change, at different excitation fluences [25].

intensity with time. This is presented in figure 4.10, for excitation at 45% of damage threshold (2 mJ/cm$^2$), by plotting the evolution of the integrated intensity of the Bragg spot as a function of time. Using the tabulated Debye-Waller factors for bulk GaAs [65], and taking into account the two-dimensionality of the surface [66], we obtained an initial temperature jump to $1565 \pm 83$ K. The system cools down on the time scale of a few hundreds of ps to reach ~510 K after 1 ns. The initial temperature jump has a rise time of 7 ps (10 ps before deconvolution). This was made possible by reducing the spatial extent of the sample to 400 $\mu$m by masking (i.e., scratching the other surface area to remove the crystal surface), resulting in a transit time of 4 ps and temporal cross-correlation of 7 ps. This rise time is in perfect agreement with results from fs optical studies of the dielectric function [50, 48]. Moreover, the maximum temperature reported above is close to the value (range of 1300 to 1500 K) extrapolated from these optical studies at corresponding fluence. For the lower fluence regime (0.4 mJ/cm$^2$) presented in figure 4.8, we find a temperature jump to $420 \pm 18$ K, with a decay leveling off at $320 \pm 5$ K after 1 ns. In this case too, the rise time and the maximum temperature are consistent with the optical study.

The evolution of the lattice expansion and that of the temperature are compared juxtaposed in figure 4.10, together with the width for the data set obtained at 2 mJ/cm$^2$. Strikingly, the temperature evolution precedes the lattice expansion and we measured a delay of 13 ps between the rise of the temperature and that of structural expansion. This lag in structural expansion provides a direct evidence for the proposed delayed lattice changes following an impulsive initial temperature [50, 48]. We note that the temperature jump to $1565 \pm 83$ K is similar to (or even exceeds) the 1513 K melting point [63], while the excitation fluence is only half of the damage threshold. However, as evident from figure 4.10, the peak temperature does not persist for a long time and the system does not loose its crystalline structure.

The lagged structural change reaches its maximum expansion of +0.025 Å at a temperature of ~1000 K (figure 4.10). This lattice expansion in nm-scale structure may now be compared with the expansion in bulk GaAs. From the linear expansion coefficient of bulk crystal [63], a temperature of 1000 K would correspond to a linear

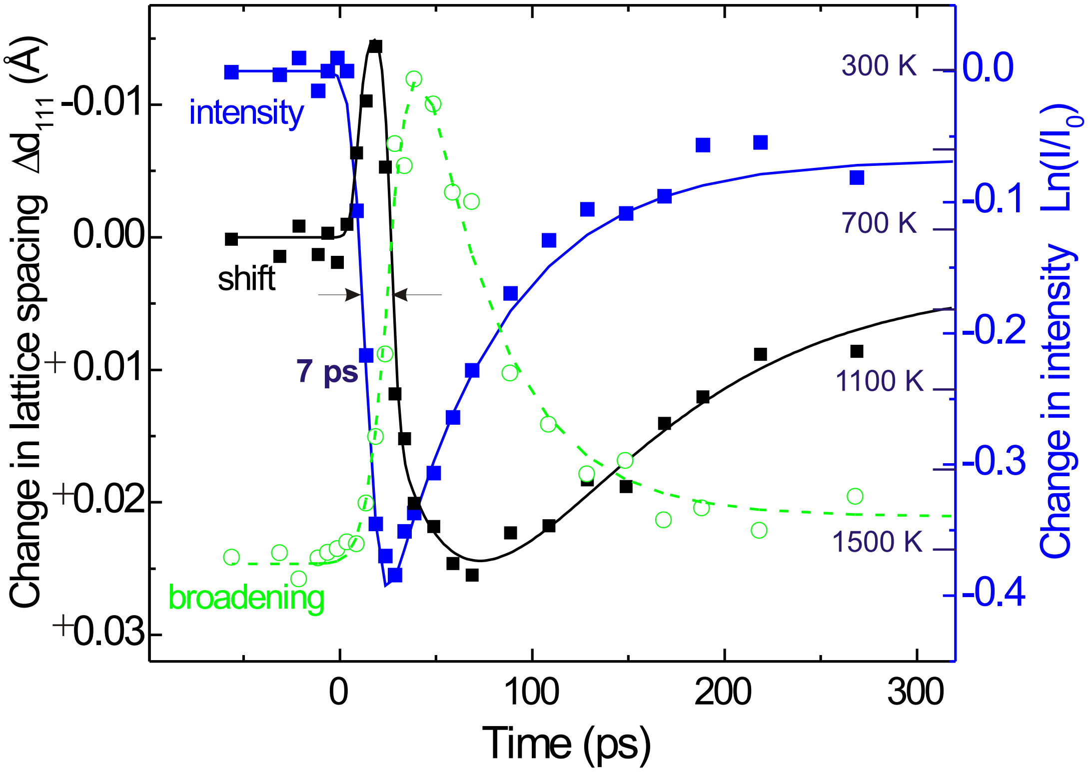

Figure 4.10: Comparison of the integrated intensity of the Bragg spot (temperature) with the change in lattice spacing for the data set obtained at 2 mJ/cm$^2$. The right axis gives the ratio of the time-dependent integrated intensity of the Bragg spot ($I$) to its counterpart at negative delay ($I_0$) on a logarithmic scale, from which the temperature scale is obtained. The lattice expansion is also shown with its scale on the left axis, together with the broadening of the Bragg spot, depicted by the dashed line. The apparent delay between the temperature rise and the lattice expansion is noted by the two arrows [25].

lattice expansion of 0.013 Å, and this value differs by a factor of two from our experimental value of 0.025 ± 0.001 Å. At much longer times (∼1 ns), when the change in expansion levels off, the temperature of 510 K would correspond to a linear expansion of 0.0038 Å and our experimental value is 0.0032 ± 0.0005 Å. This temporal decrease of the disparity in spacing is indicative of the change of surface to bulk-type behavior. From modeling of strain propagation in X-ray studies, a 0.0082 Å surface strain amplitude was inferred for GaAs [67]. Our measurement indicate a deformation larger by a factor of three.

Because of their small incidence angle, the probing electrons have a very small penetration depth (∼7 Å, for 30 keV electrons at $\theta_i \simeq 1°$) and thus probe only the very top surface layers of the crystal; in the geometry of our experiment, the excitation pulse (30° incidence angle) has a vertical penetration depth also of nm scale (3.5 nm at 266nm). These small and comparable penetration depths for the photons and for the electrons provide a unique condition for monitoring local structural dynamics of these surface layers. In X-ray experiments, a heating pulse typically has an absorption length of 0.3 $\mu$m, and the probing X-ray pulse has a $\mu$m-scale penetration depth. Such scales require consideration of strain propagation in the bulk [67]. Clearly, direct probing of the surface motions of atoms is critical to the understanding of the surface initial dynamics and to the connection to bulk propagation at different temperatures (fluences).

Additional experiments were carried out on silicon to both isolate the effect of chlorination, and also to test the generality of the approach and the scope of application. Both chlorinated and nonchlorinated silicon (111) surfaces were subjected to the same experimental conditions (excitation wavelength and fluence). Similar behavior to that of GaAs was found — while hydrogen-terminated silicon did not present noticeable surface contraction preceding the expansion (+0.06 Å), the chlorinated surface showed a prompt contraction (-0.03 Å), which precedes the expansion (+0.07 Å).

A general structural dynamics picture now emerges from the observations of the structure changes and the time scales of the motion, and from the observations on silicon surfaces. In the nonthermal regime, the initial fs transient excitation, which creates the electron-hole pairs, distorts the potential, and on the ultrashort time scale, structural changes occur by this deformation prior to significant motion in the lattice (phonons), as experimentally verified above. This highly nonequilibrium state of the solid is followed by energy dissipation and redistribution, which ultimately lead to expansion of the lattice and restructuring at longer times. With this in mind, only an expansion of the surface atoms would be expected, contrary to the observation made here of contraction and expansion. However, for the chlorine-terminated surface, the large electronegativity shifts the electronic charge distribution towards the chlorine (ionic potential). The ensuing Coulomb interaction with the underlying layers contracts the interatomic layers, as observed in the early-time ultrafast rise of the contraction, and on this time scale, the dynamics is driven by the potential change. Along with the observations made in the case of silicon and supporting this proposed mechanism for contraction, we note that atomic chlorine chemisorbed on GaAs was found to be an electron acceptor [68].

Following the contraction, expansion proceeds and on a similar time scale. Through Auger processes (at density of $\sim 10^{21}$ cm$^{-3}$), which take place in a few ps, the carrier density decreases, but the total electronic energy remains unchanged [69, 70]. The drop in the Coulombic potential along with electron-phonon coupling now drives the system in a reversed motion towards expansion. The expansion of the lattice requires 7 ps to define surface layers temperature and this is evident in the rise of the intensity profile (figure 4.10); only after this rise can we define the temperature acquired through electron-phonon coupling. The structural change (expansion) follows the temperature rise, but after an apparent delay of ~15 ps, reaching its maximum of +0.025 Å expansion at yet longer time. This thermal expansion in the (111) direction must be due to anharmonicity of lattice vibrations. Remarkably, the width of the Bragg spot reaches its maximum before the peak of structural lattice expansion. Lattice dynamics is first driven by coherent collective phonons followed by the isotropic expansion that ensues when anharmonicity becomes effective. This nascent lattice expansion must first overcome the persisting contraction. From our data, we obtained an onset for the expansion of ∼5 ps after the temperature has risen to half of its maximum and an additional delay of ∼10 ps to overcome the initial contraction. It should be noted that this picture of structural dynamics is robust at lower fluences (figure 4.9). However, in the lower fluence regime, the initial temperature is decreased, electron-phonon coupling dominates, and at longer times diffusive processes become pronounced.

The return to the original structure is observed in the decrease of $\Delta d_{111}$, from +0.025 Å to +0.003 Å, but this restructuring takes place on a much longer time scale. We note that diffusive processes must begin beyond 50 ps, as up to this time $\Delta d_{111}$ continues to increase — cooling down the surface by diffusion leads to decrease in $\Delta d_{111}$. Thus, the structure at the expanded value of $\Delta d_{111} = 0.025$ Å is vibrationally in a nonequilibrium state of collective modes, which cools down by energy redistribution and diffusion at longer times. Theoretical calculations of the heat diffusion using the known thermal properties of GaAs (heat capacity and thermal conductivity [63]) gave a good match to the temperature behavior from the point of leveling off shown in figure 4.10.

## 4.3 Surfaces with adsorbates

The single-crystal surfaces provide a template for UEC experiments to study the ultrafast dynamics of molecular adsorbates, following the ultrafast infrared (IR) laser induced temperature jump in the substrate. We studied physisorbed trifluroiodomethane on Si(111):H surfaces, water/ice on hydrophilic surfaces (chlorine terminated Si(111)) [24], and self assembled monolayer of 2-mercaptoacetic acid and iron hemes on Au(111) surfaces [27].

In the water experiment [24], we observed the coexistence of ordered surface water and crystallite-like ice structures on the nm scale, evident in the superposition of Bragg spots and Debye-Scherrer rings. The structures were determined to be dominantly cubic, but each undergoes different dynamics after the ultrafast substrate temperature jump. From changes in local bond distances with time, we elucidated the structural changes in the far-from-equilibrium regime at short times and near-equilibration at long times. However, for trifluroiodomethane on Si(111):H surfaces or self assembled monolayer on Au(111) surfaces [27], only the modulations on the substrate surface diffraction pattern were observed. Although the diffraction difference images show some structural features, it is hard to relate it to structural changes.

The challenge with these experiments is that the low density and disordering of the adsorbates, comparing to the single-crystal substrates, prevent the formation of a diffraction pattern clearly showing the structure of the molecules. While qualitatively, the diffraction patterns were shown to differ from the substrate surfaces, it is very difficult to extract quantitative structural information from the diffraction patterns. Because of the small differences, dynamical scattering theory has to be taken into account in order to analyze the diffraction patterns or to do theoretical modeling.